

# High-Throughput and Dosage-Controlled Intracellular Delivery of Large Cargos by an Acoustic-Electric Micro-Vortices Platform

Mohammad Aghaamoo, Yu-Hsi Chen, Xuan Li, Neha Garg, Ruoyu Jiang, Jeremy Tian-Hao Yun, and Abraham Phillip Lee\*

A high-throughput non-viral intracellular delivery platform is introduced for the transfection of large cargos with dosage-control. This platform, termed Acoustic-Electric Shear Orbiting Poration (AESOP), optimizes the delivery of intended cargo sizes with poration of the cell membranes via mechanical shear followed by the modulated expansion of these nanopores via electric field. Furthermore, AESOP utilizes acoustic microstreaming vortices wherein up to millions of cells are trapped and mixed uniformly with exogenous cargos, enabling the delivery of cargos into cells with targeted dosages. Intracellular delivery of a wide range of molecule sizes (<1 kDa to 2 MDa) with high efficiency (>90%), cell viability (>80%), and uniform dosages (<60% coefficient of variation (CV)) simultaneously into 1 million cells  $\text{min}^{-1}$  per single chip is demonstrated. AESOP is successfully applied to two gene editing applications that require the delivery of large plasmids: i) enhanced green fluorescent protein (eGFP) plasmid (6.1 kbp) transfection, and ii) clustered regularly interspaced short palindromic repeats (CRISPR)-Cas9-mediated gene knockout using a 9.3 kbp plasmid DNA encoding Cas9 protein and single guide RNA (sgRNA). Compared to alternative platforms, this platform offers dosage-controlled intracellular delivery of large plasmids simultaneously to large populations of cells while maintaining cell viability at comparable delivery efficiencies.

vectors are the most widely adopted intracellular delivery method in clinical applications due to their high efficiency and specificity. However, key challenges remain in terms of cytotoxicity, immunogenicity, risk of insertional toxicity, manufacturing, and limited packaging capacity.<sup>[6]</sup> Cationic lipids and polymers are among attractive non-viral candidates to replace viral methods, as they cause lower adverse immune responses and have the potential for low-cost and large-scale production. Nevertheless, low delivery efficiency for suspension cells and concerns over cytotoxicity are two major obstacles for these synthetic vectors.<sup>[7,8]</sup> Bulk electroporation is another popular non-viral method for intracellular delivery. Despite its success in the delivery of a wide range of cargos into most types of cells, including hard-to-transfect cells, high cell mortality is still a major challenge.<sup>[9–11]</sup> In addition, due to their bulk nature, cationic lipids/polymers and electroporation do not offer uniform and dosage-controlled delivery across cell populations.<sup>[12]</sup>


To address the challenges facing viral and conventional non-viral techniques,

microfluidics and nanotechnology have appeared as powerful tools that have shown tremendous potential for adoption in clinical settings and research labs.<sup>[13]</sup> Notable examples include methods based on cell deformation,<sup>[14–17]</sup> nanostructures for localized electroporation,<sup>[12,18–20]</sup> mechanoporation,<sup>[21,22]</sup>

## 1. Introduction

Intracellular delivery is an important yet challenging step in gene and cell-based therapies,<sup>[1–3]</sup> biomanufacturing,<sup>[4,5]</sup> and basic research (e.g., cell biology, drug discovery, and genetics). Viral

M. Aghaamoo, Y.-H. Chen, X. Li, N. Garg, R. Jiang, J. T.-H. Yun, A. P. Lee  
Department of Biomedical Engineering  
University of California Irvine  
Irvine, CA 92697, USA  
E-mail: aplee@uci.edu

 The ORCID identification number(s) for the author(s) of this article can be found under <https://doi.org/10.1002/adv.202102021>

© 2021 The Authors. Advanced Science published by Wiley-VCH GmbH. This is an open access article under the terms of the Creative Commons Attribution License, which permits use, distribution and reproduction in any medium, provided the original work is properly cited.

DOI: 10.1002/adv.202102021

M. Aghaamoo, Y.-H. Chen, X. Li, N. Garg, R. Jiang, A. P. Lee  
Center for Advanced Design & Manufacturing of Integrated Microfluidics (CADMIM)  
University of California Irvine  
Irvine, CA 92697, USA

J. T.-H. Yun  
Palo Alto Senior High School  
Palo Alto, CA 94301, USA

A. P. Lee  
Department of Mechanical & Aerospace Engineering  
University of California Irvine  
Irvine, CA 92697, USA

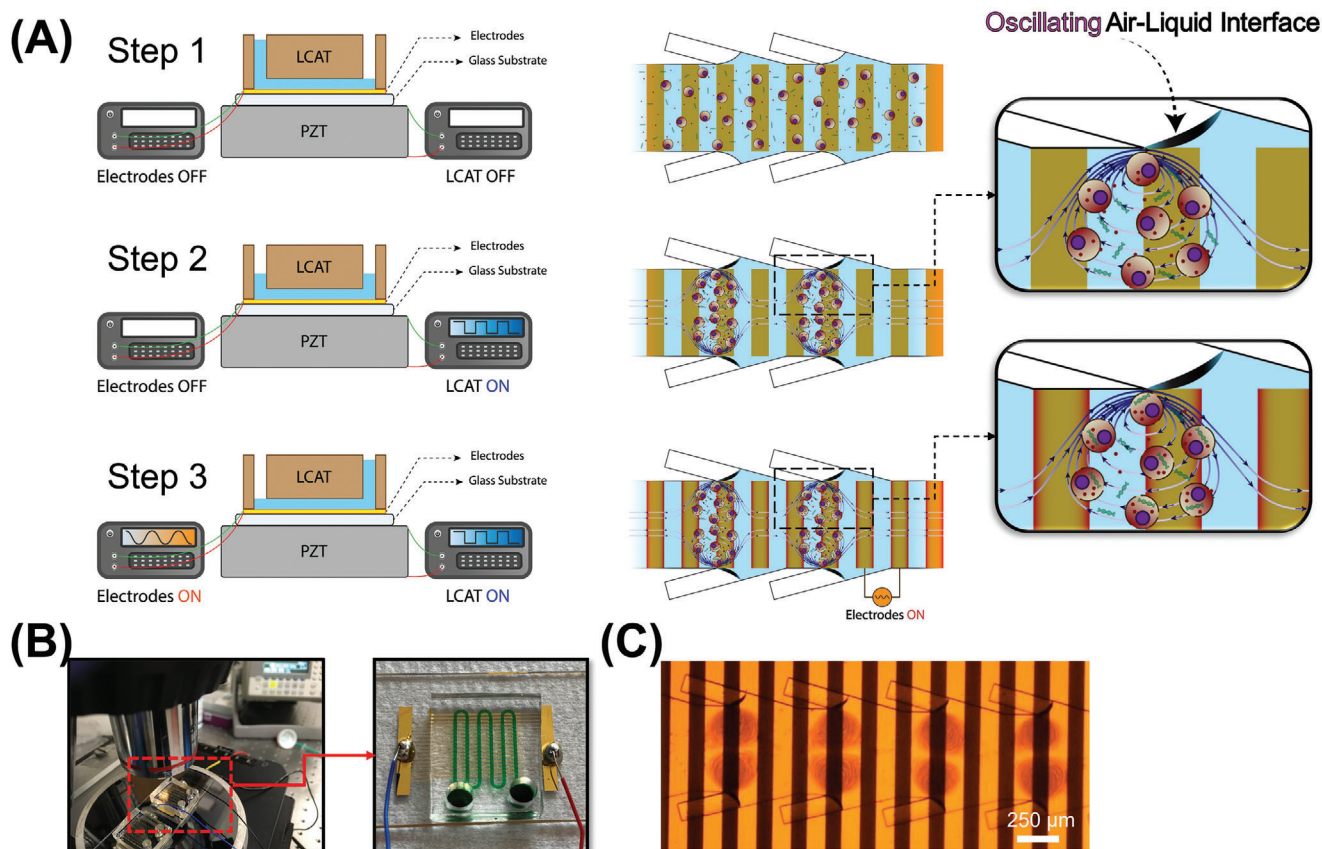


**Figure 1.** Design and operation of AESOP. A) AESOP's operational principle is based on three steps: 1) loading the cells and cargos into the chip. Once the solution primes the main channel, air-liquid interfaces will be formed between the main and side channels. 2) Turning on LCAT by applying a resonating square-wave signal to a PZT underneath the chip. The acoustic wave, transmitted from the PZT to the chip, oscillates the air-liquid interfaces, resulting in the formation of acoustic microstreaming vortices. The cells trapped in these vortices experience modest and uniform average mechanical shear that creates nanopores on their membrane. 3) Uniform enlargement of pores by uniform average exposure of the cells, rotating in vortices, to the electric field. The cargos are uniformly delivered into cells by chaotic mixing generated by acoustic microstreaming vortices. B) AESOP device setup, and C) Microscope image of cells rotating in acoustic microstreaming vortices, on top of electrodes.

acoustofluidics sonoporation,<sup>[23]</sup> flow-through electroporation,<sup>[24]</sup> droplet microfluidics,<sup>[25,26]</sup> and inertial microfluidics.<sup>[22,27]</sup> For safe, efficient, and controllable intracellular delivery, these methods focus on precise control of cellular permeabilization and uptake, down to the single-cell level. To achieve this, cells are usually treated in a 1D or 2D manner. 1D methods flow cells one-by-one and/or usually have channel dimensions at the scale of single cells,<sup>[14,22–25]</sup> while 2D methods are based on monolayer cell culturing or cell interaction with a substrate.<sup>[12,18–21]</sup> Particularly, several existing micro- and nanotechnology methods have adopted such strategies to outperform viral and conventional non-viral techniques in i) dosage-controlled delivery,<sup>[12,27–31]</sup> which enables the cell population to receive the right concentration of cargo and, thus, minimizes overdose and underdose intracellular delivery, and ii) intracellular delivery of large cargos,<sup>[15,19,32–34]</sup> which plays a key role in many genome-editing approaches such as those using clustered regularly interspaced short palindromic repeats (CRISPR)-Cas9 technology. However, these methods are either low in throughput, limited to specific cell types (e.g., adherent vs suspension cells), or complicated to operate with.

To address these limitations, here, we present an Acoustic-Electric Shear Orbiting Poration (AESOP) platform for intracellular delivery of a wide range of cargos with high efficiency, uniformity, cell viability, and throughput of 1 million cells  $\text{min}^{-1}$  per single chip. Compared to existing methods that offer intracellular delivery of large cargos and/or dosage-controlled capability, AESOP is an order of magnitude higher in throughput, compatible with both adherent and suspension cell types, and simple to operate. AESOP incorporates our lateral cavity acoustic transducer (LCAT) technology assisted by interdigitated array (IDA) electrodes for intracellular delivery (**Figure 1A–C**; and Video S1, Supporting Information). Once the cells are introduced into the platform, they are consecutively trapped in the array of acoustic microstreaming vortices generated by the LCATs. Since delivery cargos are also pumped along with the cells, they uniformly mix with cells trapped in the micro-vortices. We hypothesize 3 underlying principles of our AESOP platform: 1) cells trapped in acoustic microstreaming vortices experience modest and uniform average mechanical shear near oscillating air-liquid interfaces that opens nanopores on their cell membranes; shear-induced cell membrane poration facilitates intracellular delivery of small molecules

(<10 kDa) into cells, is cell-dependent, and can be controlled by tuning acoustic transducers, 2) rapid tumbling of cells in the streaming orbits expose them to uniform-strength electric fields that uniformly enlarges the pre-existing pores; for the formation of large pores, our two-step membrane permeabilization strategy only requires gentle and low-strength electric fields that, alone, are not effective in the absence of micro-vortices, and 3) vortices induce chaotic mixing, enabling uniform, dosage-controlled and rapid delivery of exogenous materials into the cells.

We tested the performance of AESOP with different sizes of molecules, ranging from <1 kDa to 2 MDa, and obtained >90% delivery efficiency with >80% cell viability for both adherent and suspension cell lines. In the next step, we transfected HeLa, K562, and Jurkat cells with a green fluorescent protein (GFP)-expressing plasmid (pmaxGFP, 3.5 kbp) and obtained high transfection efficiencies of >90%, >70%, and >60%, respectively, with >80% cell viability. To evaluate AESOP performance for intracellular delivery of large cargos, we first picked a 6.1 kbp enhanced green fluorescent protein (eGFP)-expressing plasmid, and could achieve >80%, >50%, and >40% transfection efficiency for HeLa, K562, and Jurkat cells, respectively, while still maintaining high cell viability of >80% for all these cell lines. Using AESOP platform, CRISPR-Cas9-mediated gene editing was demonstrated by a 9.3 kbp plasmid DNA encoding Cas9 and single guide RNA (sgRNA) to knockout phosphatase and tensin homolog deleted on chromosome 10 (PTEN) gene in K562 cells. We showed >80% intracellular delivery of CRISPR plasmid and up to 20% gene knockout across cell population. The large size of the plasmid DNA for eGFP transfection (i.e., 6.1 kbp) and CRISPR-Cas9 gene knockout (i.e., 9.3 kbp) was chosen to challenge the packaging limit of some of the common viral vectors including adeno-associated viruses (AAVs).<sup>[35]</sup> In AESOP, dosage-controlled delivery capability is achieved by the acoustic microstreaming vortices in the key steps of intracellular delivery: i) membrane disruption: by uniform average exposure to mechanical shear and electric field, and ii) cellular uptake: by uniform mixing of cells with exogenous materials. Delivery analysis of YOYO-1 labeled plasmid DNA confirmed uniform and controlled intracellular delivery across cell populations.

Compared to existing methods, our system not only can deliver a wide range of molecular sizes at high efficiency, viability, and uniformity, but it also offers unique sample processing advantages. For example, the unique design of LCATs generates a bulk flow that eliminates the need and complexity of external pumping. In addition, since cells are trapped and suspended in microstreaming vortices, the microfluidic channels are wider, making them higher throughput and less prone to clogging. Furthermore, we have demonstrated a single-chip AESOP platform at a relatively high throughput of up to 1 million cells min<sup>-1</sup> per single chip. This scalability in throughput is relatively straightforward without a reduction in system performance.

## 2. Results

### 2.1. Shear-Induced Cell Membrane Poration by Acoustic Microstreaming Vortices

To eliminate the need for applying high electric fields for intracellular delivery, AESOP initiates nanopores on the cell membrane

by mechanical shear and enlarges the pre-existing nanopores at lower electric field strengths. To achieve this, AESOP incorporates LCAT technology to trap cells inside acoustic microstreaming vortices and uniformly expose them to modest mechanical shear. The basic structural design of LCAT is illustrated in **Figure 2A** consisting of a main fluid channel with slanted dead-end side channels. Once the main channel is primed with the sample, air-liquid interfaces are formed along the channel length. When placed on a piezoelectric transducer (PZT), the acoustic energy is transmitted to the air-liquid interfaces of LCATs, causing them to oscillate and generate microstreaming vortices in the microfluidic channel. The orientation and positioning of the air-liquid cavities result in both bulk flow liquid pumping and size-selective trapping of cells.<sup>[36,37]</sup> The trapped cells orbiting in these microvortices are subjected to oscillatory mechanical shear near the oscillating air-liquid interfaces. Based on the theory developed by Nyborg for acoustic microstreaming velocity near an oscillating bubble,<sup>[38]</sup> Rooney estimated the viscous shear stress near the bubble as

$$S = \frac{2\pi^{\frac{3}{2}}\epsilon_0^2(\rho f^3 \eta)^{\frac{1}{2}}}{R_0} \quad (1)$$

where  $\rho$  is the fluid density,  $\eta$  is the fluid shear viscosity,  $f$  is the oscillation frequency,  $R_0$  is the bubble radius, and  $\epsilon_0$  is the displacement amplitude of the vibrating bubble (Figure S1 and Video S2, Supporting Information).<sup>[39–41]</sup> For the case of a moving cell rather than a stationary point near an oscillating bubble, Equation (1) can be used to estimate the upper bound of shear stress. According to Equation (1), the mechanical shear exerted on cells can be controlled by varying the interface oscillation amplitude excited by the PZT.

In the first step, particle tracking velocimetry (PTV) was employed to characterize micro-vortices and measure the velocity and trajectory of cells at different PZT applied voltages (Figure 2C,D; Figures S2–S4, Supporting Information). For all three different cell types (HeLa, K562, Jurkat) tested, although the general patterns of microstreaming vortices are similar, a higher number of Jurkat cells can be trapped per each vortex due to their smaller size ( $\approx 1200$  cells/vortex for Jurkat,  $\approx 700$  cells/vortex for HeLa and K562). This results in the formation of more streaming orbits for Jurkat cells per each vortex. The PTV results also indicate that the cells' maximum velocity is reached near the air-liquid interface (Figure 2C), and its magnitude is directly proportional to the PZT applied voltage (Figure 2D). In addition, by increasing the PZT applied voltage, the device pumping rate increases linearly (Figure S5, Supporting Information).

In the next step, we tested the hypothesis of using acoustic microstreaming vortices for shear-induced initiation of nanopores on cell membrane based on intracellular uptake of cargos with a wide range of molecular sizes. For this purpose, we introduced cells (HeLa, K562, or Jurkat) with different molecules (EthD-1 dye ( $\approx 857$  Da) or fluorescein isothiocyanate (FITC)-dextran with different sizes, ranging from 3 to 70 kDa) into the chip and activated the LCAT for 5 min (standard operation time of LCAT throughout this study). To evaluate the effect of mechanical shear force on intracellular delivery, we picked three different PZT applied voltages corresponding to “low shear (LS)” (PZT voltage = 2V,

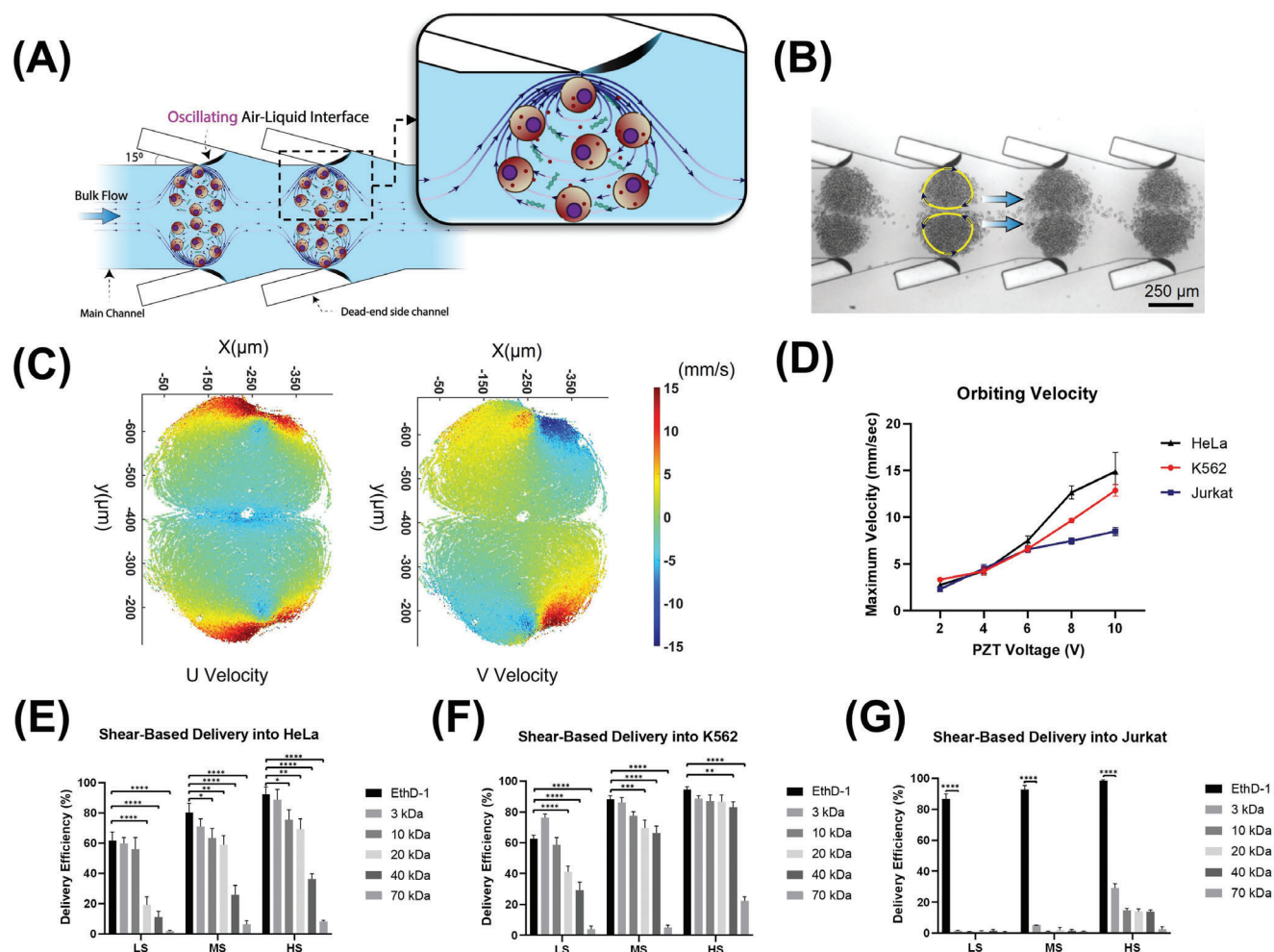


**Figure 2.** Shear-induced initiation of nanopores on cell membrane by acoustic microstreaming vortices. A) Basic design structure of LCAT technology incorporated by AESOP for shear-induced small pore formation; LCATs are arrays of acoustically actuated air-liquid interfaces generated using dead-end side channels, B) Microscope image of K562 cells trapped in acoustic microstreaming vortices generated by LCAT, C) PTV analysis results of K562 cells orbiting in acoustic microstreaming vortices (PZT voltage = 6V), D) Cells' maximum velocity orbiting in micro-vortices; the maximum velocity is reached near the air-liquid interface, and is proportional to the PZT applied voltage, E–G) Shear-induced delivery of small molecules into (E) HeLa, (F) K562, and (G) Jurkat cells at three different operational modes: “low shear (LS)” (PZT voltage = 2V), “moderate shear (MS)” (PZT voltage = 6V), and “high shear (HS)” (PZT voltage = 10V). Quantitative data were presented as mean  $\pm$  SE. For all experiments, sample size  $n = 3$ . \* $P < 0.05$ , \*\* $P < 0.01$ , \*\*\* $P < 0.001$ , and \*\*\*\* $P < 0.0001$  were determined by Tukey's honest significant difference criterion.

$S_{LS} = 4.3$  Pa, “moderate shear (MS)” (PZT voltage = 6V,  $S_{MS} = 69.4$  Pa), and “high shear (HS)” (PZT voltage = 10V,  $S_{HS} = 272.9$  Pa) (Note S1 and Video S3, Supporting Information). Based on the results (Figure 2E–G), there are four key findings: 1) Mechanical shear facilitates delivery of small molecules into the cells, indicating the formation of nano-sized pores on the cells' membrane, 2) At a given shear rate, the delivery efficiency of larger cargos is lower than smaller cargos, 3) Increasing the shear increases the delivery efficiency of molecules into the cells by creating larger pores, 4) there exists a pore size threshold for shear-induced cell membrane poration; for the three shear modes (low, moderate, and high) tested, shear alone could not deliver  $>1$  kDa molecules into Jurkat cells and  $\geq 70$  kDa molecules into HeLa and K562. Based on these results, the size of generated pores is mainly dependent on PZT applied voltage and cell type. Even though HS mode provides higher

delivery efficiency, for the rest of the studies, we chose MS mode (PZT voltage = 6V) as our optimum operational mode for LCAT. This mode offers effective small pore formation ( $>80\%$  delivery efficiency for molecules up to 3 kDa in size for K562 and HeLa, and  $>90\%$  delivery efficiency of  $\approx 857$  Da EthD-1 dye for Jurkat). Importantly, in HS mode, we observed the cell viability to drop below 80% (Figure S6, Supporting Information). This is especially important because coupling with electric field pore enlargement modality might further reduce the cell viability.

Within each acoustic microstreaming vortices, although all trapped cells experience approximately equal maximum mechanical shear near oscillating air-liquid interfaces, the cells that follow larger orbits experience lower time-averaged shear than those following the inner orbits, which results in non-uniform shearing of cells. In addition, if not controlled, some cells can escape from one vortex to another while other cells (especially

those with smaller circular paths) will be trapped in one location for the entire duration of treatment. This can also potentially contribute to inhomogeneous shear. To improve the performance of AESOP by enabling more uniform shearing of cells, PZT was turned OFF periodically (every 30 s) throughout device operation to mix and redistribute cells into different orbiting streamlines.

## 2.2. Uniform Electric Field Enlargement of Shear-Induced Pores for Cargo Delivery

Once nanopores on cells' membrane are initiated by acoustic microstreaming vortices, AESOP enlarges the pores by applying a sinusoidal alternating current (AC) electric field via IDA electrodes. For each different cell type, electric field voltage, frequency, and applied time were optimized (Note S2 and Figures S7–S9, Supporting Information). Specifically, we found  $12.5 V_{\max}$  ( $|E|_{\text{RMS}} = 0.4 \text{ kV cm}^{-1}$ ), 10 kHz, and 10 ms for HeLa cells,  $35 V_{\max}$  ( $|E|_{\text{RMS}} = 0.99 \text{ kV cm}^{-1}$ ), 30 kHz, and 10 ms for K562 cells, and  $25 V_{\max}$  ( $|E|_{\text{RMS}} = 0.85 \text{ kV cm}^{-1}$ ), 20 kHz, and 10 ms for Jurkat cells, as the optimum electric field parameters. Numerical modeling was used to calculate the applied field strengths ( $|E|$ ) corresponding to each different electric field voltages (Note S3 and Figures S10–S12, Supporting Information). We, then, tested the performance of AESOP in delivery of dextran with molecular sizes ranging from 3 kDa to 2 MDa (Figure 3A). According to the results, for all three different cell lines tested, >90% delivery efficiency was achieved for any given molecular size of dextran.

In the next step, to evaluate the role of shear in AESOP performance, we fixed the optimum applied electric field parameters for each cell type and compared AESOP with: 1) Flow-through: with LCAT off, the cells were flown through the chip and on top of the electrodes using a syringe pump, 2) Static: with LCAT off, the cells were loaded into the chip and settled down on top of the electrodes, and 3) LCAT Only: with LCAT on and electrodes off, the cells were loaded into the chip to be trapped in acoustic microstreaming vortices and experience mechanical shear with no electric field. Based on the results (Figure 3C), compared to AESOP, flow-through and static groups that use only electric fields (LCAT off) are inefficient at intracellular delivery of large molecules in the absence of mechanical shearing. Specifically, the results for delivery of 2 MDa dextran (Figure 3D–F) indicate that AESOP achieves significantly higher delivery efficiency (>90%) compared to flow-through (low, <30%) and static (moderate, <60%). The moderate delivery efficiency of static approach is because the cells are close to or in contact with the electrodes and, thus, experience high electric field strengths (Note S3 and Figure S12, Supporting Information). Like bulk electroporation, the exposure to a high electric field in a static approach is particularly unfavorable for applications that long-term cell viability is critical after the delivery process (e.g., plasmid and mRNA delivery).

## 2.3. Dosage-Controlled Capability and Mechanism of Intracellular Delivery

In AESOP platform, acoustic microstreaming vortices play a key role in the efficient and precise intracellular delivery of cargos. The cells in these vortices are not only exposed to uniform average mechanical shear and electric field, but also uniformly mixed

with exogenous cargos by chaotic mixing. Thus, we hypothesized that the imposed uniformity in membrane disruption and cellular uptake would result in dosage-controlled intracellular delivery across cell population. To test this hypothesis, we delivered YOYO-1 labeled plasmid DNA (6.1 kbp) into K562 cells using AESOP and two other control groups (static and flow-through). Since the amount of plasmid DNA delivered to a cell is directly proportional to the measured fluorescent intensity of YOYO-1 dye within the cell, fluorescent intensity distribution among the cell population was analyzed by flow cytometry. According to the histogram of fluorescent intensity (Figure 4A), AESOP offers a narrow peak distribution of YOYO-1 labeled DNA, indicating delivery of uniform doses across the cell population. In contrast, for the two control groups, where the effect of vortices was eliminated by turning LCAT off, the intensity peak distribution of delivered DNA is wide and not uniform among the population of cells.

To better quantify controllable intracellular delivery, we calculated the percentage coefficient of variation (%CV, defined as the percentage ratio of standard deviation to the mean) of fluorescent intensity across cell populations processed by the control groups and AESOP with DNA concentrations of 50 ng, 500 ng, 1  $\mu\text{g}$ , and 2.5  $\mu\text{g}$  per million cells (Figure 4B). Unlike the two control groups with %CV>120, all AESOP groups offer %CV around 50%. We also compared the performance of AESOP with a commercial electroporation system (Lonza Nucleofector). According to the results (Figure S13, Supporting Information), AESOP reduces the %CV by half compared to the Lonza Nucleofector. The low %CV achieved by AESOP groups not only confirms delivery of uniform doses across the cell population, but also is an indicator of performance consistency when working with different cargo concentrations.

In addition, for each different DNA concentration, we calculated the mean fluorescent intensity of YOYO-1 dye delivered to the cells (Figure 4C). Based on the results, the average dose delivered to the cells is linearly proportional to DNA concentration, indicating that AESOP offers controllable intracellular delivery. We also evaluated how cargo size would affect the uniformity of intracellular delivery across cell populations. For this purpose, we calculated the %CV for intracellular delivery of 3.5 kbp, 6.1 kbp, and 9.3 kbp plasmids. The results (Figure S14, Supporting Information) show that AESOP offers a low and consistent %CV of intracellular delivery regardless of cargo size.

In the next step, we investigated whether high-throughput cell processing affects the performance of AESOP for gene delivery. For this, two different AESOP designs were tested with the same DNA concentration: 1) moderate throughput: capable of processing up to 200K cells  $\text{min}^{-1}$  (Figure 1B,C), and 2) high throughput: capable of processing up to 1M cells  $\text{min}^{-1}$  (Figure S15 and Video S4, Supporting Information). Based on the results (Figure 4D,E), except for overdose delivery into a small percentage ( $\approx 5\%$ ) of cells in the high-throughput version, there is no significant difference in delivery efficiency and uniformity between the two versions. This indicates that the scalability of the platform is straightforward and does not significantly affect system performance. Figure 4F shows the corresponding efficiency and cell viability for delivery of labeled plasmid into cells. Similar to the trend observed in intracellular delivery of 2 MDa dextran, the results indicate that both moderate and high-throughput AESOP versions

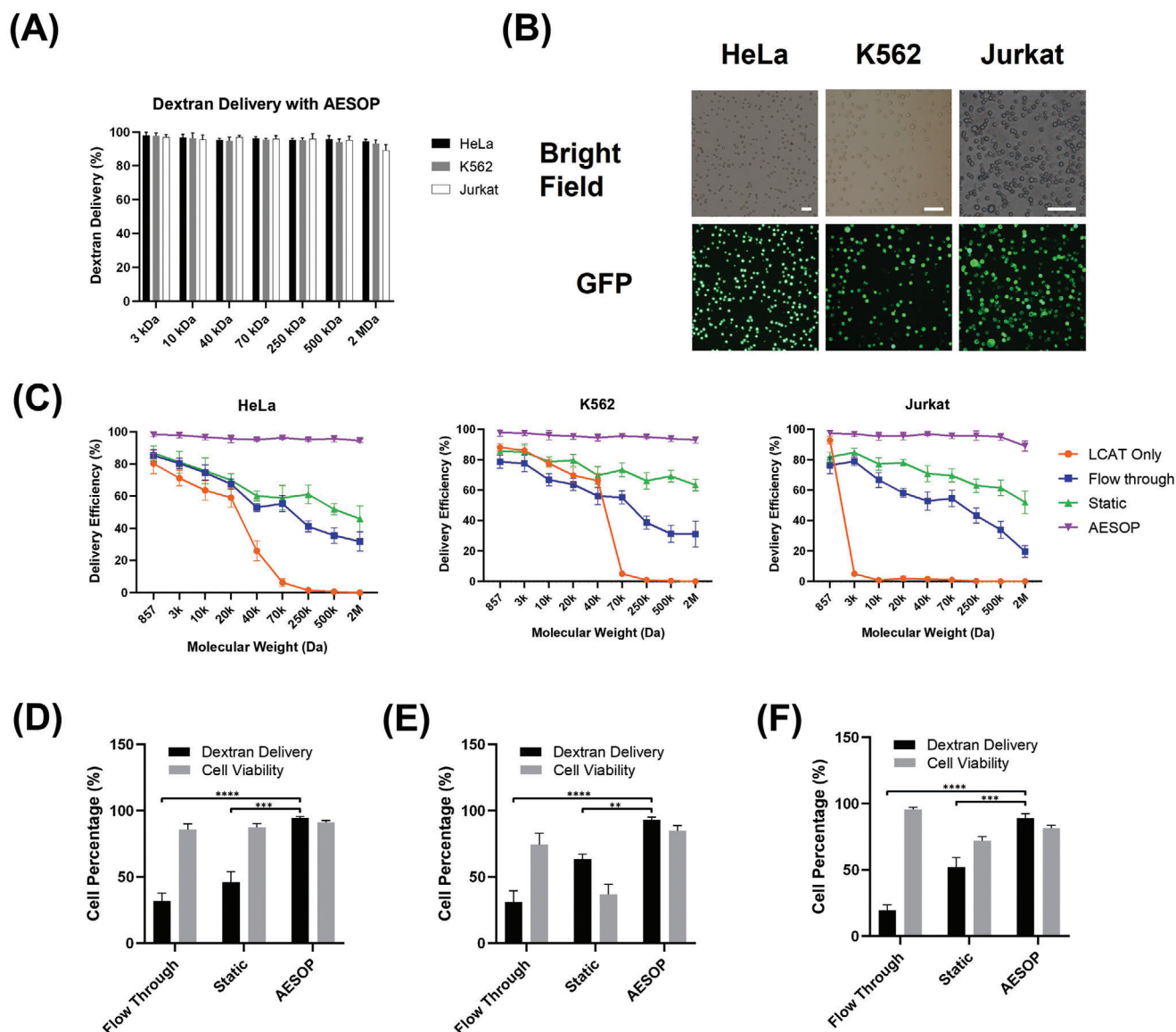


**Figure 3.** AESOP for intracellular delivery of different sizes of cargo. A) Performance of AESOP in delivery of dextran, with a wide range of molecular size, into HeLa, K562, and Jurkat cell lines, B) Brightfield and GFP image of HeLa, K562, and Jurkat cells tested for delivery of 2 MDa dextran with AESOP platform, C) Comparison of the performance of the AESOP with “Flow-through”, “Static”, and “LCAT only” in delivery of a wide range of molecular sizes (EthD-1 dye ( $\approx 857$  Da) or FITC-dextran with different sizes, ranging from 3 kDa to 2 MDa), D–E) Comparison of the performance of the AESOP with “Flow-through” and “Static” in delivery of 2 MDa dextran and corresponding cell viability for (D) HeLa, (E) K562, and (F) Jurkat; the results indicate that AESOP offers significantly higher delivery efficiency compared to the “Flow-through” and “Static” groups. Quantitative data were presented as mean  $\pm$  SE. For all experiments, sample size  $n = 3$ . \* $P < 0.05$ , \*\* $P < 0.01$ , \*\*\* $P < 0.001$ , and \*\*\*\* $P < 0.0001$  were determined by Tukey’s honest significant difference criterion. The scale bars in (B) are 100  $\mu\text{m}$ .

achieve high delivery efficiency of plasmid (>80%) while static and flow-through control groups result in <60% and <30% efficiency, respectively.

In the next step, we evaluated how AESOP facilitated the intracellular delivery of plasmid DNA into cells. The main question was whether LCAT entangles the plasmid DNA to the cell membrane,<sup>[42]</sup> or delivers directly to either the cytoplasm or nucleus.<sup>[18,43]</sup> For this purpose, cells’ nuclei and membranes were labeled with DAPI and CellMask plasma membrane stains, respectively. After the experiment, confocal microscopy was per-

formed to observe the distribution of labeled plasmid DNA in K562 cells. Based on the results (Figure 4G), the plasmid DNA is mostly delivered into the cells’ cytoplasm. Since AESOP utilizes AC electric field with frequencies  $\geq 10\text{kHz}$ , the effect of DNA electrophoresis can be neglected. This indicates that the chaotic mixing induced by microstreaming vortices acts as the major active force to guide the plasmid DNA through the cell membrane, and into the cytoplasm. As a result, LCAT eliminates the need for any other active force, such as electrophoresis, to guide DNA into the cells.

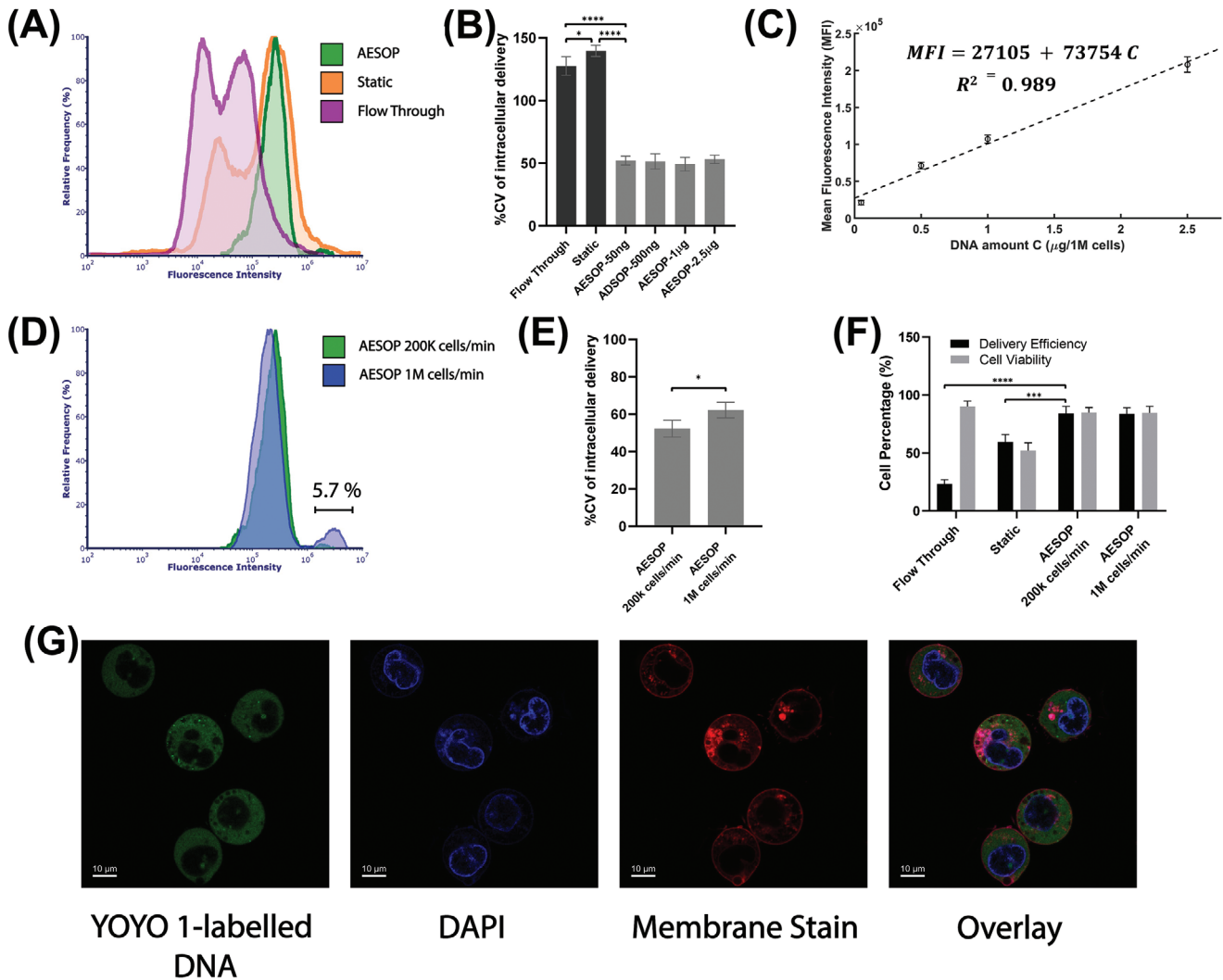


**Figure 4.** Intracellular delivery of fluorescently labeled plasmid DNA A) Histogram of fluorescent intensity of YOYO-1 labeled plasmid DNA delivered into K562 cells. For better comparison, the histograms were normalized by relative frequency (%). Compared to control groups, AESOP offers a sharp and narrow intensity distribution, indicating AESOP's capability for precise and controlled delivery, B) %CV of intracellular delivery for control groups (flow-through and static) and AESOP operated with different DNA concentrations, C) Mean fluorescent intensity of YOYO-1 dye delivered to the cells by AESOP operated with different DNA concentrations. A linear model is fitted to the obtained data, indicating controlled delivery by AESOP, D) The histogram of fluorescent intensity of YOYO-1 labeled plasmid DNA delivered into K562 cells using moderate and high throughput AESOP platforms, E) %CV of intracellular delivery for moderate and high-throughput AESOP versions; increasing the throughput resulted in a slight increase in delivery distribution across cell population, F) The Delivery efficiency and cell viability for intracellular delivery of labeled DNA into cells; the results show that >80% plasmid DNA delivery efficiency can be achieved using AESOP platform, and G) Confocal microscopy image of cells after intracellular delivery experiment with AESOP; for this experiment, the cells' nuclei and membranes were stained with DAPI and deep red CellMask plasma membrane stains. Based on the results, acoustic microstreaming vortices directly deliver the plasmid DNA to the cell cytoplasm. Quantitative data were presented as mean  $\pm$  SE. For all experiments, sample size  $n = 3$ . \* $P < 0.05$ , \*\* $P < 0.01$ , \*\*\* $P < 0.001$ , and \*\*\*\* $P < 0.0001$  were determined by One-way ANOVA with Tukey's honest significant difference criterion for (B) and (F), and student t-test for (E).

#### 2.4. Gene Delivery Analysis: eGFP Plasmid DNA Transfection & CRISPR-Cas9 Gene Editing

We also explored the performance of AESOP for intracellular gene delivery applications in protein expression and targeted gene knockout. First, we transfected HeLa, Jurkat, and K562 cells with a  $\approx 3.5$  kbp GFP-expressing plasmid (pmaxGFP). The protein expression levels were analyzed by flow cytometry 48 h after the gene delivery experiments. Based on the results (Figure 5A;

Figure S16, Supporting Information), high GFP protein expression efficiencies of >90%, >60%, and >70% were obtained for HeLa, Jurkat, and K562 cells, respectively, with cell viability of >80% for all the three cell types tested. In the next step, a relatively large eGFP-expressing plasmid DNA (6.1 kbp) was chosen and delivered into cells using the AESOP platform. For this large eGFP plasmid, we could achieve >80%, >40%, and >50% transfection efficiencies for HeLa, Jurkat, and K562, respectively, while still maintaining cell viability to be >80% (Figure 5B,C). To rule

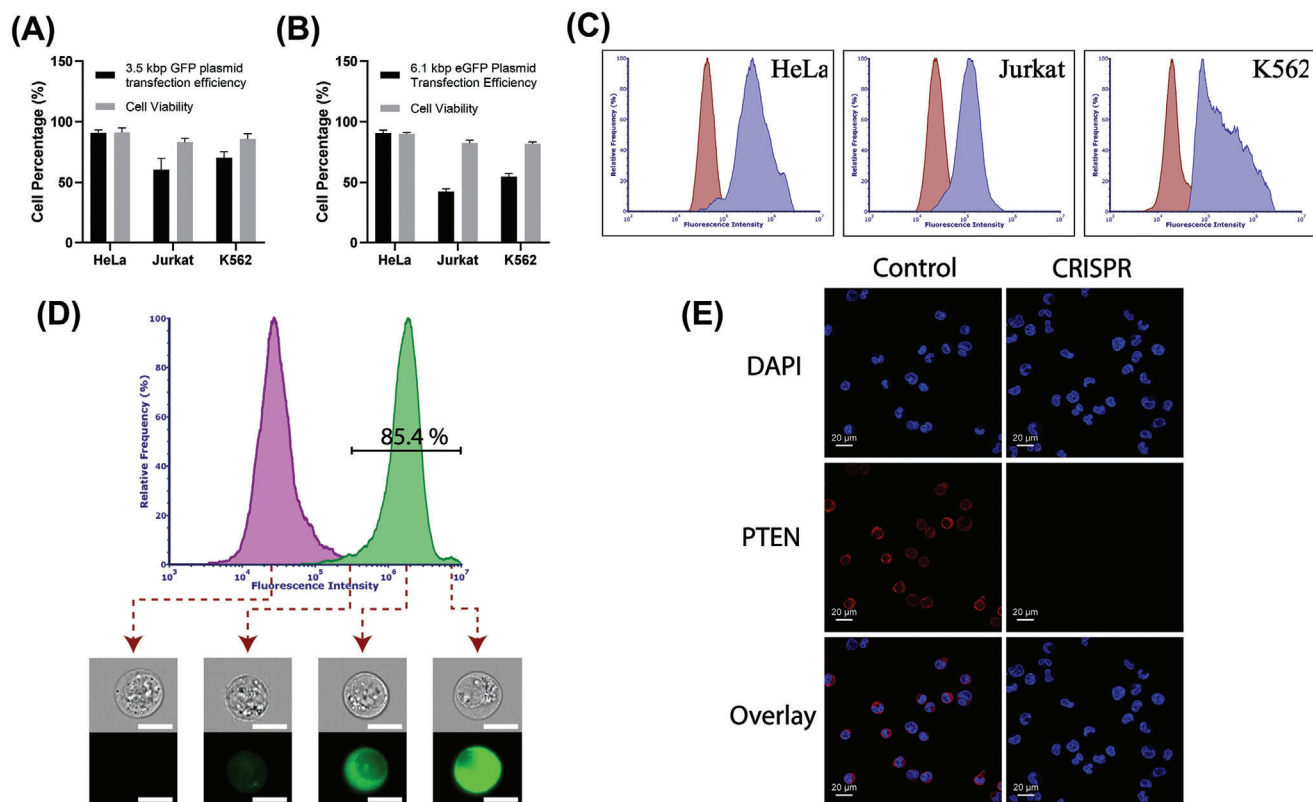


**Figure 5.** Gene delivery analysis. A) Transfection efficiencies and cell viability 48 h after delivery of 3.5 kbp GFP-expressing plasmid DNA; AESOP achieved >90%, >60%, and >70% transfection efficiencies with >80% high cell viabilities, B) Transfection efficiencies and cell viability 48 h after delivery of 6.1 kbp eGFP-expressing plasmid DNA; AESOP achieved >80%, >40%, and >50% transfection efficiencies with >80% high cell viabilities, C) Flow cytometry quantification of eGFP expression for experimental (blue) and control (red) groups. The cells in control group were incubated for 48 h with plasmid DNA, D) Flow cytometry quantification of delivery of YOYO-1 labeled plasmid DNA encoding Cas9 protein and PTEN sgRNA into K562 cells for experimental (green) and control (purple) groups. Plasmid DNA was mixed with the cell sample in the control group. For better comparison, the histograms were normalized by relative frequency (%), E) IF staining of K562 cells with PTEN monoclonal antibody recognized by Alexa Fluor 647 secondary antibody. DAPI was used to stain the nucleus. The scale bars in (D) are 10  $\mu$ m.

out the possibility that AESOP is only an electroporator coupled with mixing provided by acoustic microstreaming vortices, we performed K562 cell transfection with 6.1 kbp eGFP plasmid using a “Static” approach (loading the cells on top of electrodes and applying the same optimized E parameters) followed by immediately turning on acoustic microstreaming vortices to perform mixing. According to the results (Figure S17, Supporting Information), without shear-induced initiation of nanopores before applying an electric field, very low transfection efficiency ( $\approx$ 5%) was achieved.

We then evaluated AESOP for CRISPR-Cas9 gene editing applications. For this purpose, a 9.3 kbp plasmid DNA encoding Cas9 protein and sgRNA targeting PTEN gene knockout were chosen and delivered into K562 cells. Based on the flow cytometry analysis of cells treated with AESOP, CRISPR-plasmid intracellular delivery efficiencies of >80% were achieved for K562 cells (Figure 5D). After gene delivery, the cells were cultured for 48 h, selected with eGFP marker (up to 20% of cell population were eGFP positive with >80% viability), cultured for an additional 7 days, and analyzed by immunofluorescence (IF) staining. Compared to the control group, where PTEN proteins were detected in the cytoplasm, the experimental group showed a clear knock-

out of the gene (Figure 5E). Thus, based on the eGFP marker, we estimate up to 20% gene knockout via AESOP platform, which requires future confirmation by comprehensive DNA sequencing analysis. No significant changes were observed in cell viability for 48 h and 7 days culture.

As a proof-of-concept, we also tested AESOP for transfection of human primary T cells. Based on our preliminary results, we could achieve up to 30% GFP protein expression efficiency and >80% cell viability (Figure S18, Supporting Information). To further enhance AESOP performance in engineering primary T cells, the next stage of our research involves a more in-depth optimization of mechanical shear and electric field parameters.

### 3. Discussion and Conclusion

AESOP is a multimodal non-viral intracellular delivery platform that meets the key criteria needed for adoption in gene/cell-based therapies, biomanufacturing, and basic research. These criteria include: i) High delivery efficiency while maintaining cell viability, ii) Dosage-controlled delivery of cargos, iii) High throughput, iv) Compatibility with both adherent and suspension cell types, and v) Simplicity in fabrication and operational protocol. For this,



AESOP controls cell membrane permeabilization and cellular uptake in an efficient, precise, and high-throughput manner.

To permeabilize cell membranes effectively and gently, AESOP adopts a two-step membrane disruption strategy that uniquely combines two robust and well-known cell-membrane mechanical-disruption approaches: mechanical shear and electroporation.<sup>[13,44,45]</sup> First, it forms nanopores on the cell membrane using mechanical shear. Second, it enlarges these nanopores upon the cells' uniform exposure to gentle electric fields. Stable bubble oscillations have been known to apply local shear force and permeabilize nearby cells by inducing localized deformation on the plasma membrane.<sup>[46–50]</sup> Similar to this principle, AESOP employs LCAT's acoustic microstreaming vortices to apply tuned and moderate mechanical shear on cells near oscillating air-liquid interfaces and, consequently, creates nanopores on their membrane. As pore resealing occurs in the order of milliseconds to seconds,<sup>[47,51,52]</sup> detection of pores by techniques such as scanning electron microscopy<sup>[53]</sup> or atomic force microscopy<sup>[54]</sup> imaging is challenging due to the long preparation time required. Thus, in this study, we relied on intracellular uptake of different sizes of molecules to confirm the formation of pores and estimate their sizes. One of our important findings indicates that shear-induced cell membrane poration is cell type dependent. This can be explained by the fact that each cell type has different mechanical properties (e.g., cell membrane stiffness and cytoskeleton arrangement) and, consequently, experiences different shear-induced localized membrane deformation near the oscillating air-liquid interfaces.<sup>[49,55]</sup> To open larger pores, AESOP needs only gentle and low-strength, rather than undesirable high-strength, electric fields. We hypothesize that by shear-induced transient formation of nanopores, AESOP does not need to apply a high electric field to overcome large transmembrane threshold potential to create hydrophobic pores. Instead, we speculate that only a low electric field is required to expand the pre-existing hydrophobic pores to lower-energy hydrophilic pores without creating new pores.<sup>[56]</sup> This strategy is indeed similar to dual-pulse electroporation strategy where the cells experience a short, high-strength pulse followed by a long, low-strength pulse. The former creates several nanopores on the cell membrane, and the latter expands the pores and electrophoretically guides the charged cargos into the cell.<sup>[57,58]</sup> This strategy has been shown to improve delivery efficiency and cell viability.<sup>[13]</sup> AESOP outperforms dual-pulse electroporation technique because it does not rely on high-strength pulse to initiate the creation of nanopores. As a result, it overcomes fundamental challenges of using high-strength electric fields in electroporation such as joule heating, metal contamination, electrolysis, and pH change in buffer. In addition, since cells are tumbling in acoustic microstreaming vortices, they are uniformly exposed to both mechanical shear and electric field, resulting in uniform membrane permeabilization across the cell population.

In terms of cellular uptake, AESOP uses chaotic mixing, induced by acoustic microstreaming vortices, to deliver cargos efficiently and uniformly into cells. The majority of intracellular delivery approaches rely on either passive diffusion or electrophoresis to guide the cargos into cells. Compared to passive diffusion, electrophoresis significantly improves the intracellular delivery of cargos into permeabilized cells. Recently, micro-vortices have

also been shown to enhance cellular uptake by mixing cells with the exogenous cargos.<sup>[24,25,27]</sup> In our previous work, we developed a droplet microfluidic platform for lipid-mediated single-cell transfection. We showed that chaotic advection, formed inside droplets moving in a winding channel, can significantly enhance cell transfection efficiency and uniformity.<sup>[25]</sup> Here, in AESOP, we took a new approach for high-throughput and efficient mixing, and designed hundreds of whirlpool-like microstreaming vortices to simultaneously mix hundreds of thousands of permeabilized cells with exogenous cargos. Our presented results indicate the important role of these vortices to increase cellular uptake efficiency.

As a result of uniform average exposure to both mechanical shear and electric field as well as uniform cellular uptake, AESOP offers dosage-controlled delivery capability. This is an important requirement for many cell engineering applications. For example, Mali et al. showed that precise control over Cas9-sgRNA dose is critical for achieving desired targeting specificity in Cas9 gene editing.<sup>[59]</sup> In this paper, we evaluated dosage-controlled intracellular delivery by flow cytometry analysis of the cells processed by AESOP. We used %CV as an indicator of relative dispersion of the amount of DNA delivered to the cell population and showed that %CV < 60 can be achieved by AESOP. In the next step, AESOP performance was evaluated at different DNA concentrations (Figure 4B,C). We found out that: i) %CV is independent of the cargo concentration and size, showing the performance consistency, and ii) the average dose delivered to individual cells is linearly proportional to the cargo concentration. Utilizing this precise intracellular delivery approach, we could lower the cargo concentration, down to 1  $\mu$ g of plasmid per million cells. This is particularly important for reducing the cost and minimizing toxicity associated with plasmids.<sup>[60]</sup> Overall, several promising micro- and nanotechnology approaches have been developed for dosage-controlled intracellular delivery such as nanostraw-electroporation,<sup>[12]</sup> nanofountain probe electroporation,<sup>[28]</sup> nanochannel electroporation,<sup>[29]</sup> micro/nano-injection,<sup>[30,31]</sup> cell-induced acoustic microstreaming,<sup>[61]</sup> and microscale symmetrical electroporator arrays.<sup>[27]</sup> Compared to these methods, AESOP is an order of magnitude higher in throughput and compatible with both suspension and adherent cells, as cells are suspended in acoustic microstreaming vortices. Building on this foundation, future research will be focused on further enhancing the uniformity of membrane permeabilization and cellular uptake. In our current AESOP version, it is reasonable to assume that the streaming flow has a 2D profile.<sup>[62]</sup> As a result, cells orbiting in different orbits will experience different time-averaged mechanical shear. To circumvent this, here we periodically turned off the LCAT (needs to be further optimized) to redistribute cells into different orbits and achieve uniform time-averaged mechanical shearing. As an alternative strategy, in effective 3D vortices, not only better mixing can be achieved, but also the cells' shearing is more uniform due to the widening and tightening of the orbits along the height of the microchannel. In future experiments, we will explore the effects of channel dimensions (especially the height), oscillation mode, amplitude, and frequency of air-liquid interface, and cells' size on enhancing the 3-D streaming.<sup>[62]</sup>

In recent years, there has also been a growing need for intracellular delivery of large cargos for gene editing. For example,

most plasmid-based CRISPR-Cas9 gene editing cargos are >9 kbp. Another powerful recent development is base editing, which uses a cytosine base editor or an adenine base editor with a guide RNA and, as a result, requires delivery of complexes with an approximate size of 6 kbp.<sup>[63]</sup> For these applications, the use of viral vectors is challenging due to their limited packaging capacity. For example, AAVs, as popular vectors for gene/cell-based therapies, have a packaging capacity of 4.7 kbp and, thus, dual or triple AAV delivery approaches are required for cargos that exceed such a limit.<sup>[63,64]</sup> Recently, methods based on membrane deformation,<sup>[15]</sup> bubble cavitation,<sup>[32,33]</sup> nanochannel electroporation,<sup>[19]</sup> and high-frequency ultrasound<sup>[34]</sup> have demonstrated successful delivery of large cargos (>6 kbp). Despite encouraging results, compared to AESOP, these methods are lower in throughput and/or require cell interaction with a substrate that limits their application mostly to adherent cells. Our presented results with 6.1 kbp eGFP plasmid and 9.3 kbp CRISPR-Cas9 plasmid show that AESOP also addresses two other key challenges associated with the delivery of large cargos: low delivery efficiency and cell viability. Overall, it is more challenging to deliver larger cargos, as diffusion-limited intracellular delivery becomes extremely inefficient. One solution is to increase the cargo concentration to achieve acceptable transfection efficiency. Thus, for large cargos, not only are larger pores needed, high concentration of cargos greatly reduces the cells' viability, in particular for plasmid-based gene editing applications as there exists specific toxicity associated with large plasmids.<sup>[60]</sup> The chaotic advection provided by AESOP not only increases the transport of larger cargo molecules to overcome their lower diffusion rates, but it also reduces the required concentration of cargos to minimize overdose delivery across cell populations.

For adoption in clinical settings, intracellular delivery platforms should also satisfy the requirement for high-throughput cell processing. As an example, Tisagenlecleucel (Kymriah), the anti-CD19 chimeric antigen receptor (CAR) T-cell therapy for pediatric patients with B-cell precursor acute lymphoblastic leukemia, requires an average dose of  $1 \times 10^8$  transduced viable T cells.<sup>[65]</sup> Our current  $2 \text{ cm} \times 5 \text{ cm}$  high-throughput AESOP chip can already process up to 1 million cells  $\text{min}^{-1}$  (<1 h for processing  $1 \times 10^8$  cells). It should be noted that several promising microfluidic platforms can process cells with the same throughput or higher.<sup>[66–68]</sup> However, compared to these methods, AESOP's presented capabilities in uniform and dosage-controlled intracellular delivery of cargos at such level of throughputs make it an attractive candidate to be used in clinical settings. In this work, by comparing moderate ( $200 \text{ k cells min}^{-1}/\text{chip}$ ) and high-throughput ( $1 \text{ M cells min}^{-1}/\text{chip}$ ) AESOP versions, we demonstrated the scalability of our platform without sacrificing the delivery efficiency and precision across cell populations. This is mainly because AESOP consists of hundreds of micro-vortices, each holding thousands of cells, that act as independent reactors. With flow control and optimization, our next step will be focused on achieving 10 million cells  $\text{min}^{-1}$  (<10 min for processing  $1 \times 10^8$  cells). This would require optimization of the microfluidic channels and LCATs to maximize cell processing density and speed. Increasing the channel dimensions (length, width, and height) is the most direct way to increase throughput. However, this may require an increase in PZT applied voltage or duration of operation. As a result, careful attention should be

paid to PZT-induced local heating and bubble stability over the duration of operation. In this work, under optimum operational parameters (PZT voltage = 6V, applied time = 5 min), we did not observe significant PZT-induced local heating or instability in the air-liquid interfaces (Note S4 and Figures S19 and S20, Supporting Information). As an alternative strategy to increase system throughput, parallelization of multiple chips (stacking) would be also adopted. One of the intrinsic advantages of the AESOP technology is that the whole system is compact with pumping, trapping, shearing, and interdigitated electrodes, all on one common microfluidic chip platform. Consequently, the whole system is simple, easy to operate, test, and characterize.

## 4. Experimental Section

**Materials and Reagents:** Dulbecco's modified Eagle's medium (DMEM), fetal bovine serum (FBS), Iscove's modified Dulbecco's medium (IMDM), Roswell Park Memorial Institute (RPMI) 1640, Dynabeads CD3/CD28, and Human interleukin-2 (IL-2) Recombinant Protein (Invitrogen) were purchased from Thermo Fisher Scientific. HeLa, K562, and Jurkat (human acute T cell leukemia cell line) cells were purchased from American Tissue Culture Collection (ATCC; Manassas, VA). ImmunoCult-XF T Cell Expansion Medium was purchased from STEMCELL Technologies. FITC-dextran molecules were purchased from MilliporeSigma. pcDNA3.1+C-eGFP plasmid and plasmid encoding Cas9 and sgRNA were purchased from GenScript. For PTEN targeted gene knockout experiment, the 20bp sgRNA sequence of TTATCCAACAT-TATTGCTA was used. YOYO-1 dye (1 mM solution in DMSO; Invitrogen, cat. no. Y3601), DAPI (4',6-diamidino-2-phenylindole) stain, CellMask Deep Red Plasma membrane Stain, PTEN Monoclonal Antibody, and Goat anti-Mouse IgG (H+L) Highly Cross-Adsorbed Secondary Antibody, Alexa Fluor Plus 647 were purchased from Thermo Fisher Scientific.

**Device Fabrication:** AESOP integrates IDA electrodes with LCAT chip (Figure S21, Supporting Information). Lift-off technique was adopted for batch electrode fabrication. For this, the glass slides were, first, cleaned with acetone, isopropyl alcohol, and methanol, and dried overnight at 120 °C. Standard photolithography, using MICROPOSIT S1813 positive photoresist, was performed to fabricate patterns on the glass slides. Using e-beam evaporation, 300°A chromium (Cr) followed by 1000°A gold (Au) were deposited on the slides. The Cr layer was chosen to improve the adhesion of Au layer to the substrate. After thin film deposition, the glass slides were sonicated in a bath of acetone to remove the photoresist and, subsequently, stripping away unwanted metal layers. Soft lithography technique was employed for the fabrication of the LCAT chip. For this, negative photoresist SU-8 2050 (Kayaku Advanced Materials, Inc.) was used for pattern fabrication on a silicon wafer. The silicon wafer was then silanized overnight by (TRIDECAFLUORO-1,1,2,2-TETRAHYDROOCTYL)TRICHLOROSILANE (Gelest, Inc.) to avoid PDMS-mold adherence. Poly (dimethylsiloxane), PDMS (Sylgard 184, Dow Corning) base, and curing agent were mixed at the ratio of 10:1, poured on the mold, degassed for 1 h in a desiccator, and cured at 65 °C overnight. The cured PDMS was peeled from the wafer, cut to size, and cleaned. Both the LCAT chip and glass slide, with patterned electrodes, were aligned and bonded by oxygen plasma treatment. Finally, to make the AESOP device hydrophobic, it was baked overnight at 65 °C.

**Standard AESOP Operation and Intracellular Delivery Protocol:** For efficient transport of acoustic waves from PZT to the device, an ultrasound gel (Aquasonic) was first smeared between the AESOP chip and the PZT (STEMiNC, STEINER & MARTINS, Inc., Resonant frequency = 50.2 kHz). The PZT and AESOP chip were separately connected to a signal generator (Agilent 33220A) and a power amplifier (JUNTEK). The cell solution was suspended in electroporation buffer (Bio-Rad Laboratories, Inc.), mixed with the desired concentration of exogenous cargos (e.g., dextran, eGFP plasmid, CRISPR plasmid, etc.), and pipetted into the device inlet in 30  $\mu\text{L}$

sample batches. For pumping the sample into the chip and applying tunable mechanical shear to the cells, the PZT was then excited by a square wave at a fixed frequency of 50.2 kHz and the desired amplitude. For electrical expansion of shear-induced pores on cells' membrane, while cells orbiting in acoustic microstreaming vortices, a sinusoidal wave was applied three times (with 30 s intervals) to the IDA electrodes with the desired frequency, amplitude, and duration. It should be mentioned that throughout 5 min device operation, LCATs were turned OFF periodically (every 30 s) for uniform mechanical shearing of cells and better mixing of cells with cargos. After delivery, the cells were collected from the device and recovered in a cell culture medium without FBS for 20 min. After recovery, the cells were dispersed in their respective culture media supplemented with 10% FBS and incubated in a humidified atmosphere of 5% CO<sub>2</sub>/95% air at 37 °C.

**Cell Culture:** HeLa cells were grown in DMEM supplemented with 10% FBS. K562 cells were grown in IMDM supplemented with 10% FBS. Jurkat cells were grown in RPMI 1640 medium supplemented with 10% FBS. All cells were cultured in a humidified atmosphere of 5% CO<sub>2</sub>/95% air at 37 °C.

**Primary T Cell Isolation and Culture Protocols:** Whole blood samples from healthy donors were obtained from Institute for Clinical & Translational Science (ICTS) at the University of California Irvine. Within 12 h following blood collection, primary T cells were isolated using immunomagnetic negative selection kits (STEMCELL Technologies). After isolation, they were suspended with (PBS)-washed Dynabeads CD3/CD28 at a cell-to-bead ratio of 1:1. Isolated T cells and Dynabeads were cultured in ImmunoCult-XF T Cell Expansion Medium with 30 U mL<sup>-1</sup> Human IL-2 Recombinant Protein at 37 °C in a humidified 5% CO<sub>2</sub> incubator for 3 days. The seeding density of T cells was 1 × 10<sup>6</sup> cells mL<sup>-1</sup>.

**Labeling Plasmid DNA, Immunofluorescence (IF) Staining, Flow Cytometry, and Confocal Laser Scanning Microscopy:** For studying mechanism, efficiency, and uniformity of intracellular delivery, plasmid DNA was labeled with YOYO-1 dye at a ratio of 1 dye molecule per 5 bp of the DNA.<sup>[24]</sup> For this, the desired concentration of plasmid DNA was mixed with the YOYO-1 dye and incubated for 1 h at room temperature in the dark. The fluorescently labeled DNA was then mixed with the cell sample and intracellular delivery was performed. After sample collection, the cells were washed three times in 1X PBS to remove background and any nonspecifically adsorbed plasmid DNA from the cell surface. The cells were then resuspended in 1X PBS for flow cytometry and confocal laser scanning microscopy.

IF analysis was adopted to evaluate the CRISPR-Cas9-mediated targeted gene knockout efficiency. For this, the cells were first fixed using 4% formaldehyde (pH 7.4) (Polysciences, Inc.) for 10 min at room temperature. Then, they were permeabilized by 0.1% Triton X-100 (ICN Biomedicals, Inc.) in 1X phosphate-buffered saline (PBS) for 15 min at room temperature and blocked with 3% bovine serum albumin (BSA) in PBST (PBS+ 0.1% Tween 20) for 30 min at room temperature. Cells were then probed with the diluted primary PTEN antibody in 1% BSA in PBST (1:10 dilution ratio) overnight at 4 °C. They were then incubated with the secondary antibody (5 μg mL<sup>-1</sup>) in 1% BSA for 1 h at room temperature in the dark. The cells were then resuspended in 1X PBS and plated on a microscope slide for confocal laser scanning microscopy. In between all the IF steps, the cells were washed in 1X PBS three times.

Flow cytometry was performed by an ImageStream Mark II Imaging Flow Cytometer (Amnis Corporation) at 60 × magnification under the laser excitation of 488 nm. Confocal laser scanning microscopy was performed by a ZEISS LSM 700 laser scanning confocal microscope (Carl Zeiss) with a 63x oil objective and three laser lines: 405nm for DAPI, 488nm for YOYO-1 labeled plasmid, and 639nm for detecting Alexa Fluor Plus 647 secondary antibodies.

**Particle Tracking Velocimetry (PTV) Analysis:** Cells' motion in acoustic microstreaming vortices was captured using a high-speed camera (Phantom, vision research) connected to a L150 Nikon Eclipse upright microscope. For improved particle detection, high pass filter was used for edge detection. The video was then analyzed by an open-source MATLAB code to track the cells and obtain their velocity components in microstreaming vortices.<sup>[69]</sup>

**Cell Viability Test:** The Calcein Red AM (AAT Bioquest) was used to determine the cell viability. For analysis, the cells were resuspended in 1x PBS buffer (ThermoFisher Scientific) and a stock solution of Calcein Red AM was added to the cells' solution with 1:100 volume ratio. The flow cytometry was used to evaluate the viability.

**Statistical Analysis:** Quantitative data were presented as mean ± standard error (SE). For all experiments, unless otherwise stated, n = 3. The error bars were obtained by technical replicates. Statistical analyses were performed using MATLAB. Student t-test, One-way ANOVA, and multiple comparison with Tukey's honest significant difference criterion were performed to evaluate the statistical significance of differences. *P* < 0.05 was considered as statistically significant (\**P* < 0.05, \*\**P* < 0.01, \*\*\**P* < 0.001, and \*\*\*\**P* < 0.0001) and *P* > 0.05 as nonsignificant (ns).

The percentage coefficient of variation (%CV) of fluorescent intensity of YOYO-1 dye delivered to the cell population were calculated on at least 95% of YOYO-1 dye positive (gated) cell population as:

$$\%CV = \frac{SD}{\mu} \times 100 \quad (2)$$

where SD and  $\mu$  are standard deviation and mean of fluorescent intensity, respectively.

## Supporting Information

Supporting Information is available from the Wiley Online Library or from the author.

## Acknowledgements

M.A. and Y.-H.C. contributed equally to this work. The authors would like to acknowledge support from the National Science Foundation and the Center for Advanced Design and Manufacturing of Integrated Microfluidics (NSF I/UCRC award number IIP 1841509).

## Conflict of Interest

M.A., X.L., N.G., Y.-H.C., and A.P.L. are inventors on a US patent application filed by the University of California, Irvine, relating to the acoustic-electric micro-vortices platform.

## Data Availability Statement

The data that supports the findings of this study are available in the Supporting Information of this article.

## Keywords

CRISPR-Cas9, intracellular delivery, large cargo, precise-dose delivery

Received: May 16, 2021  
Revised: September 23, 2021  
Published online: October 29, 2021

- [1] N. P. Restifo, M. E. Dudley, S. A. Rosenberg, *Nat. Rev. Immunol.* **2012**, *12*, 269.
- [2] A. D. Fesnak, C. H. June, B. L. Levine, *Nat. Rev. Cancer* **2016**, *16*, 566.
- [3] M. L. Maeder, C. A. Gersbach, *Mol. Ther.* **2016**, *24*, 430.

- [4] O.-W. Merten, S. Charrier, N. Laroudie, S. Fauchille, C. Dugué, C. Jenny, M. Audit, M.-A. Zanta-Boussif, H. Chautard, M. Radrizzani, G. Vallanti, L. Naldini, P. Noguez-Hellin, A. Galy, *Hum. Gene Ther.* **2010**, *22*, 343.
- [5] L. Baldi, D. L. Hacker, M. Adam, F. M. Wurm, *Biotechnol. Lett.* **2007**, *29*, 677.
- [6] K. Lundstrom, *Diseases* **2018**, *6*, 42.
- [7] M. A. Mintzer, E. E. Simanek, *Chem. Rev.* **2009**, *109*, 259.
- [8] H. Lv, S. Zhang, B. Wang, S. Cui, J. Yan, *J. Controlled Release* **2006**, *114*, 100.
- [9] P. J. Canatella, J. F. Karr, J. A. Petros, M. R. Prausnitz, *Biophys. J.* **2001**, *80*, 755.
- [10] T. B. Napotnik, T. Polajžer, D. Miklavčič, *Bioelectrochemistry* **2021**, *141*, 107871.
- [11] T. Geng, C. Lu, *Lab Chip* **2013**, *13*, 3803.
- [12] Y. Cao, H. Chen, R. Qiu, M. Hanna, E. Ma, M. Hjort, A. Zhang, R. S. Lewis, J. C. Wu, N. A. Melosh, *Sci. Adv.* **2018**, *4*, eaat8131.
- [13] M. P. Stewart, R. Langer, K. F. Jensen, *Chem. Rev.* **2018**, *118*, 7409.
- [14] A. Sharei, J. Zoldan, A. Adamo, W. Y. Sim, N. Cho, E. Jackson, S. Mao, S. Schneider, M.-J. Han, A. Lytton-Jean, P. A. Basto, S. Jhunjhunwala, J. Lee, D. A. Heller, J. W. Kang, G. C. Hartoularos, K.-S. Kim, D. G. Anderson, R. Langer, K. F. Jensen, *Proc. Natl. Acad. Sci. U. S. A.* **2013**, *110*, 2082.
- [15] X. Han, Z. Liu, M. C. Jo, K. Zhang, Y. Li, Z. Zeng, N. Li, Y. Zu, L. Qin, *Sci. Adv.* **2015**, *1*, e1500454.
- [16] J. Yen, M. Fiorino, Y. Liu, S. Paula, S. Clarkson, L. Quinn, W. R. Tschantz, H. Klock, N. Guo, C. Russ, V. W. C. Yu, C. Mickanin, S. C. Stevenson, C. Lee, Y. Yang, *Sci. Rep.* **2018**, *8*, 16304.
- [17] M. T. Saung, A. Sharei, V. A. Adalsteinsson, N. Cho, T. Kamath, C. Ruiz, J. Kirkpatrick, N. Patel, M. Mino-Kenudson, S. P. Thayer, R. Langer, K. F. Jensen, A. S. Liss, J. C. Love, *Small* **2016**, *12*, 5873.
- [18] Y. Cao, E. Ma, S. Cestellos-Blanco, B. Zhang, R. Qiu, Y. Su, J. A. Doudna, P. Yang, *Proc. Natl. Acad. Sci. U. S. A.* **2019**, *116*, 7899.
- [19] L. Chang, P. Bertani, D. Gallego-Perez, Z. Yang, F. Chen, C. Chiang, V. Malkoc, T. Kuang, K. Gao, L. J. Lee, W. Lu, *Nanoscale* **2016**, *8*, 243.
- [20] P. Mukherjee, S. S. P. Nathamgari, J. A. Kessler, H. D. Espinosa, *ACS Nano* **2018**, *12*, 12118.
- [21] H. G. Dixit, R. Starr, M. L. Dundon, P. I. Pairs, X. Yang, Y. Zhang, D. Nampe, C. B. Ballas, H. Tsutsui, S. J. Forman, C. E. Brown, M. P. Rao, *Nano Lett.* **2020**, *20*, 860.
- [22] Y. Deng, M. Kizer, M. Rada, J. Sage, X. Wang, D.-J. Cheon, A. J. Chung, *Nano Lett.* **2018**, *18*, 2705.
- [23] J. N. Belling, L. K. Heidenreich, Z. Tian, A. M. Mendoza, T.-T. Chiou, Y. Gong, N. Y. Chen, T. D. Young, N. Wattanatorn, J. H. Park, L. Scarbelli, N. Chiang, J. Takahashi, S. G. Young, A. Z. Stieg, S. De Oliveira, T. J. Huang, P. S. Weiss, S. J. Jonas, *Proc. Natl. Acad. Sci. U. S. A.* **2020**, *117*, 10976.
- [24] T. Geng, Y. Zhan, J. Wang, C. Lu, *Nat. Protoc.* **2011**, *6*, 1192.
- [25] X. Li, M. Aghaamoo, S. Liu, D.-H. Lee, A. P. Lee, *Small* **2018**, *14*, 1802055.
- [26] B. Joo, J. Hur, G.-B. Kim, S. G. Yun, A. J. Chung, *ACS Nano* **2021**, *15*, 12888.
- [27] M. Ouyang, W. Hill, J. H. Lee, S. C. Hur, *Sci. Rep.* **2017**, *7*, 44757.
- [28] W. Kang, F. Yavari, M. Minary-Jolandan, J. P. Giraldo-Vela, A. Safi, R. L. McNaughton, V. Parpoil, H. D. Espinosa, *Nano Lett.* **2013**, *13*, 2448.
- [29] P. E. Boukany, A. Morss, W.-c. Liao, B. Henslee, H. Jung, X. Zhang, B. Yu, X. Wang, Y. Wu, L. Li, K. Gao, X. Hu, X. Zhao, O. Hemminger, W. Lu, G. P. Lafyatis, L. J. Lee, *Nat. Nanotechnol.* **2011**, *6*, 747.
- [30] Y. T. Chow, S. Chen, R. Wang, C. Liu, C.-w. Kong, R. A. Li, S. H. Cheng, D. Sun, *Sci. Rep.* **2016**, *6*, 24127.
- [31] E. Shekaramiz, G. Varadarajalu, P. J. Day, H. K. Wickramasinghe, *Sci. Rep.* **2016**, *6*, 29051.
- [32] Y.-C. Wu, T.-H. Wu, D. L. Clemens, B.-Y. Lee, X. Wen, M. A. Horwitz, M. A. Teitell, P.-Y. Chiou, *Nat. Methods* **2015**, *12*, 439.
- [33] J. Cai, S. Huang, Y. Yi, S. Bao, *J. Int. Med. Res.* **2019**, *47*, 2199.
- [34] S. Yoon, P. Wang, Q. Peng, Y. Wang, K. K. Shung, *Sci. Rep.* **2017**, *7*, 5275.
- [35] D. Wang, P. W. L. Tai, G. Gao, *Nat. Rev. Drug Discovery* **2019**, *18*, 358.
- [36] A. R. Tovar, A. P. Lee, *Lab Chip* **2009**, *9*, 41.
- [37] N. Garg, T. M. Westerhof, V. Liu, R. Liu, E. L. Nelson, A. P. Lee, *Microsyst. Nanoeng.* **2018**, *4*, 17085.
- [38] W. L. M. Nyborg, in *Physical Acoustics*, (Ed: W. P. Mason), Academic Press, New York **1965**, p. 265.
- [39] J. A. Rooney, *Science* **1970**, *169*, 869.
- [40] J. A. Rooney, *J. Acoust. Soc. Am.* **1972**, *52*, 1718.
- [41] J. Wu, J. P. Ross, J.-F. Chiu, *J. Acoust. Soc. Am.* **2002**, *111*, 1460.
- [42] T. Y. Tsong, *Biophys. J.* **1991**, *60*, 297.
- [43] X. Ding, M. P. Stewart, A. Sharei, J. C. Weaver, R. S. Langer, K. F. Jensen, *Nat. Biomed. Eng.* **2017**, *1*, 0039.
- [44] M. B. Fox, D. C. Esveld, A. Valero, R. Luttmann, H. C. Mastwijk, P. V. Bartels, A. van den Berg, R. M. Boom, *Anal. Bioanal. Chem.* **2006**, *385*, 474.
- [45] J. Olofsson, K. Nolkranz, F. Ryttsén, B. A. Lambie, S. G. Weber, O. Orwar, *Curr. Opin. Biotechnol.* **2003**, *14*, 29.
- [46] P. Marmottant, S. Hilgenfeldt, *Nature* **2003**, *423*, 153.
- [47] A. van Wamel, K. Kooiman, M. Harteveld, M. Emmer, F. J. ten Cate, M. Versluis, N. de Jong, *J. Controlled Release* **2006**, *112*, 149.
- [48] L. Meng, X. Liu, Y. Wang, W. Zhang, W. Zhou, F. Cai, F. Li, J. Wu, L. Xu, L. Niu, H. Zheng, *Adv. Sci.* **2019**, *6*, 1900557.
- [49] I. Lentacker, I. De Cock, R. Deckers, S. C. De Smedt, C. T. W. Moonen, *Adv. Drug Delivery Rev.* **2014**, *72*, 49.
- [50] B. D. M. Meijering, L. J. M. Juffermans, A. v. Wamel, R. H. Henning, I. S. Zuhorn, M. Emmer, A. M. G. Versteilen, W. J. Paulus, W. H. v. Gilst, K. Kooiman, N. d. Jong, R. J. P. Musters, L. E. Deelman, O. Kamp, *Circ. Res.* **2009**, *104*, 679.
- [51] Y. Zhou, J. Cui, C. X. Deng, *Biophys. J.* **2008**, *94*, L51.
- [52] C. X. Deng, F. Sieling, H. Pan, J. Cui, *Ultrasound Med. Biol.* **2004**, *30*, 519.
- [53] F. Yang, N. Gu, D. Chen, X. Xi, D. Zhang, Y. Li, J. Wu, *J. Controlled Release* **2008**, *131*, 205.
- [54] Y.-Z. Zhao, Y.-K. Luo, C.-T. Lu, J.-F. Xu, J. Tang, M. Zhang, Y. Zhang, H.-D. Liang, *J. Drug Targeting* **2008**, *16*, 18.
- [55] E. M. Darling, D. Di Carlo, *Annu. Rev. Biomed. Eng.* **2015**, *17*, 35.
- [56] T. Kotnik, L. Rems, M. Tarek, D. Miklavčič, *Annu. Rev. Biophys.* **2019**, *48*, 63.
- [57] S. I. Sukharev, V. A. Klenchin, S. M. Serov, L. V. Chernomordik, A. C. Yu, *Biophys. J.* **1992**, *63*, 1320.
- [58] Y. Demiryurek, M. Nickaen, M. Zheng, M. Yu, J. D. Zahn, D. I. Shreiber, H. Lin, J. W. Shan, *Biochim. Biophys. Acta, Biomembr.* **2015**, *1848*, 1706.
- [59] P. Mali, K. M. Esvelt, G. M. Church, *Nat. Methods* **2013**, *10*, 957.
- [60] L. L. Lesueur, L. M. Mir, F. M. André, *Mol. Ther.–Nucleic Acids* **2016**, *5*, e291.
- [61] A. Salari, S. Appak-Baskoy, I. R. Coe, J. Abousawan, C. N. Antonescu, S. S. H. Tsai, M. C. Kolios, *Lab Chip* **2021**, *21*, 1788.
- [62] A. Marin, M. Rossi, B. Rallabandi, C. Wang, S. Hilgenfeldt, C. J. Kähler, *Phys. Rev. Appl.* **2015**, *3*, 041001.
- [63] H. A. Rees, D. R. Liu, *Nat. Rev. Genet.* **2018**, *19*, 770.
- [64] C. L. Xu, M. Z. C. Ruan, V. B. Mahajan, S. H. Tsang, *Viruses* **2019**, *11*, 28.
- [65] S. L. Maude, T. W. Laetsch, J. Buechner, S. Rives, M. Boyer, H. Bittencourt, P. Bader, M. R. Vermeris, H. E. Stefanski, G. D. Myers, M. Qayed, B. De Moerloose, H. Hiramatsu, K. Schlis, K. L. Davis, P. L. Martin, E. R. Nemecek, G. A. Yanik, C. Peters, A. Baruchel, N. Boissel, F. Mechinaud, A. Balduzzi, J. Krueger, C. H. June, B. L. Levine, P. Wood, T. Taran, M. Leung, K. T. Mueller, Y. Zhang, K. Sen, D.

- Lebwohl, M. A. Pulsipher, S. A. Grupp, *N. Engl. J. Med.* **2018**, 378, 439.
- [66] J. Brooks, G. Minnick, P. Mukherjee, A. Jaber, L. Chang, H. D. Espinosa, R. Yang, *Small* **2020**, 16, 2004917.
- [67] C. A. Lissandrello, J. A. Santos, P. Hsi, M. Welch, V. L. Mott, E. S. Kim, J. Chesin, N. J. Haroutunian, A. G. Stoddard, A. Czarnecki, J. R. Coppeta, D. K. Freeman, D. A. Flusberg, J. L. Balestrini, V. Tandon, *Sci. Rep.* **2020**, 10, 18045.
- [68] M. E. Kizer, Y. Deng, G. Kang, P. E. Mikael, X. Wang, A. J. Chung, *Lab Chip* **2019**, 19, 1747.
- [69] J. Heyman, *Comput. Geosci.* **2019**, 128, 11.